Progress in Reaction Kinetics and Mechanism

ARTICLE

Open Access

https://doi.org/10.48130/prkm-0026-0020

Progress in Reaction Kinetics and Mechanism **2026**, 51: e026

Synergistic enhancement of sintering resistance and tar cracking over Ni/Ce-doped CaO for biomass gasification: DFT and experimental study

Xianyao Yan[1,2], Boxin Ding[1], Chenyu Duan[3], Fang Liu[2*], Xinyan Zhou[2], Weipeng Deng[1] and Huaqiang Chu[1*]

[1] *School of Energy and Environment, Anhui University of Technology, Maanshan 243002, China*
[2] *State Key Laboratory of Continential Shale Oil, Daqing 163000, China*
[3] *School of Energy and Environment, Southeast University, Nanjing 210096, China*
* Correspondence: xiaofangqqq@163.com (Liu F); hqchust@163.com (Chu H)

Abstract

The sorption-enhanced biomass gasification with CaO-based materials exhibits considerable potential for simultaneous CO_2 mitigation and hydrogen generation. However, activity attenuation of CaO-based materials over extended cyclic processes has limited their industrial applications. In this work, the improvement in cyclic stability of the materials is enhanced by Ni/Ce doping, and the sintering kinetics and tar cracking mechanisms are elucidated using combined density functional theory with experimental investigations. The results demonstrate that doping with Ni and Ce is found to reduce the band gap and introduce new states neighboring the Fermi level, which facilitate electron migration to stabilize reaction transition states. Therefore, the intrinsic kinetic barrier is reduced. The formation energies of the doped surfaces are significantly reduced, indicating enhanced intrinsic stability. Ca_4O_4 cluster adsorption is used to assess sintering resistance, which reveals that Ni aggravates sintering, while Ce stabilizes the lattice and suppresses Ni agglomeration. Cyclic CO_2 capture tests indicate that Ni doping enhances initial activity, while Ce doping effectively suppresses high-temperature sintering, and high CO_2 capture performance is obtained during 20 cycles. Toluene is physically adsorbed on the surfaces, and its adsorption energy is nearly doubled by doping. The ring-opening of toluene is calculated to be the rate-determining step on the CaO-based material surfaces, and the activation barrier is reduced by Ni and Ce doping. The synergistic incorporation of Ni and Ce balances catalytic reactivity and structural stability; thus, Ni/Ce-doped CaO exhibits promising potential to obtain high sintering resistance and tar cracking performance.

Keywords: CaO-based material, CO_2 capture, Biomass gasification, Tar cracking, Reaction kinetics, Density functional theory

Citation: Yan X, Ding B, Duan C, Liu F, Zhou X, et al. 2026. Synergistic enhancement of sintering resistance and tar cracking over Ni/Ce-doped CaO for biomass gasification: DFT and experimental study. *Progress in Reaction Kinetics and Mechanism* 51: e026 https://doi.org/10.48130/prkm-0026-0020

Introduction

The greenhouse effect has been aggravated by the rising anthropogenic CO_2 emissions, and the consumption of fossil fuels has been widely acknowledged as the primary contributor to the emissions[1]. The Intergovernmental Panel on Climate Change suggested that annual CO_2 emissions are expected to reach 48 Gt by 2050 in the absence of effective interventions[2]. Consequently, CO_2 capture and storage is regarded as critical to relieve anthropogenic CO_2 emissions and achieve carbon neutrality. Owing to the advantages of transportability and cleanliness, hydrogen is recognized as one of the most appropriate candidates among the energy carriers[3]. Presently, the large-scale production of hydrogen remains dependent on thermochemical conversion of fossil fuels[4].

Gasification of biomass is deemed promising because of the biogas acquisition, low transportation costs, and carbon neutrality[5]. Due to the incorporation of CaO-based materials into the sorption-enhanced gasification of biomass, CO_2 absorption can be accomplished, as expressed by Eq. (1)[6]. Therefore, the gasification system is driven towards improved H_2 generation by the disruption of the reaction equilibrium[7]. The formed calcium carbonate during gasification can be subsequently shifted to the calciner, and elevated temperatures are used to drive its decomposition into CaO and CO_2[8]. The obtained CaO is recirculated back towards the gasifier to continue the following gasification reaction. In this manner, CO_2 absorption via calcium looping and hydrogen production can be coupled within one process; thus, elevated H_2 production is maintained[9]. Furthermore, the exothermic nature of CO_2 absorption of CaO-based materials can partially offset the heat duty of the gasifier, which reduces the net energy consumption of biomass gasification. However, as the number of the cycle increases, CO_2 absorption capacities of CaO-based materials suffer from severe decrease, resulting from the sintering and coke deposition from tar generation[10,11]. The improvement in H_2 production during the cycles is accordingly weakened because of the limited cyclic performance of CaO-based materials[12]:

$$C_nH_mO_p + (2n-p)H_2O + nCaO \rightarrow nCaCO_3 + (\frac{m}{2} + 2n - p)H_2 \quad (1)$$

To overcome inherent limitations of CaO-based materials for steam gasification of biomass, particularly severe thermal sintering and lack of catalytic activity for tar degradation, the development of CaO-based materials by incorporating transition metals and inert supports has been proposed in previous studies[13]. Among various catalysts, Ni has been widely recognized as highly active and cost-effective for C–C and C–H bond breaking; thus, it is considered a primary choice for *in-situ* tar cracking and methane reforming. Quan et al.[14] fabricated Ni-doped CaO material with the sol-gel technique, which achieved high H_2 production and cyclic stability during steam reforming of ethanol. This material was conducive to reduced carbon deposition, and the elongated CNTs were the dominant deposited carbon. The effect of synthesis methods on CO_2 capture characteristics of Ni-CaO dual-functional materials was

https://doi.org/10.48130/prkm-0026-0020

investigated by Wang et al.[15]. Pretreatment with organic acids like propionic acid and complexation with citric acid enhanced both the surface features and dispersion of Ni species in the doped CaO material, and superior structural characteristics were obtained with the citric acid-assisted approach. The favorable CO_2 capture performance was correlated with improved textural properties, reduced particle dimensions, and homogeneous distribution of Ni species. Sun et al.[16] found that the morphology of CaO-based material could be significantly enhanced by the Ni loading. The contribution of Ni-Ca interactions was found to be limited, which could be ascribed to poor reducibility and accessibility. It was observed that a higher Ni loading led to increased carbon deposition, while stable CO_2 capture of approximately 10–13 mmol/g per cycle was achieved at a Ni loading of 10 wt% under 650 °C, and the optimal reaction performance was obtained. However, under high-temperature calcination conditions, rapid deactivation is inevitably induced in Ni-doped CaO materials, which is attributed to the severe agglomeration of both the active Ni particles and the CaO framework, as well as heavy coke deposition by which the active sites are blocked[17]. Therefore, the introduction of a structural promoter is significant to enhance sintering resistance and suppress coking. CeO_2 is regarded as an ideal promoter because of its elevated Tammann temperature and the redox effects from the coexistence of Ce^{3+}/Ce^{4+} pairs, which are known to boost reaction activity. Consequently, CeO_2 is regarded as a suitable promoter for CaO-based materials[18–20]. Wang et al.[21] found that Ce-doped CaO delivered improved sintering resistance, which was ascribed to the porous, shell-interconnected cross-linked microstructure and the high stability. The facile interconversion between Ce^{3+} and Ce^{4+} was shown to generate a charge imbalance, which therefore created oxygen vacancies and unsaturated chemical bonds in the material. As a result, CO_2 absorption of 0.59 g/g was maintained at the 18th cycle by the Ce-doped CaO material, and an enhanced carbonation rate was also achieved. Consequently, through strong metal-support interactions, the porous structure for stable CO_2 capture can be preserved, and the electronic properties of Ni can be modulated in Ni/Ce co-doped CaO materials, thereby improving H_2 production and tar cracking performance.

Density functional theory (DFT) calculations, as an effective technique to elucidate chemical reactions at the atomic scale, have been applied to investigate CO_2 absorption[22], water-gas shift[23], CO_2 reduction[24], and hydrogen storage[25]. Shi et al.[26] investigated the sintering resistance of Cr and Co-doped CaO materials on the surfaces. The presence of Co and Cr shortened the metal-oxygen distance, and the activation barrier for oxygen vacancy generation was reduced. Upon Ca_4O_4 cluster adsorption, the generation of stronger metal–oxygen bonds in the materials could inhibit particle fusion. Wang et al.[27] reported that Ca_4O_4 cluster adsorption energy on the pristine CaO surface was significantly weakened by Ni doping. In contrast, the adsorption of Ca_4O_4 clusters on the substrate is strengthened by Al_2O_3, as reflected by the E_{ad} of −7.34 eV; thus, cluster deformation is restrained, and the sintering of CaO grains is further suppressed. Moreover, DFT calculations on sintering resistance in terms of Ca_4O_4 adsorption have been performed on Ti/Ni co-doped CaO[28], Al-doped CaO[29], and Mn-doped CaO[30] surfaces, indicating the feasibility. Wang et al.[31] performed DFT calculations on toluene molecule adsorption and ring opening on the Fe/Ni co-doped CaO surface. The results indicated that toluene decomposition on this surface was more difficult than on Fe- and Ni-solely doped CaO surfaces. Zou et al.[32] studied the effects of an Si co-doped CaO surface for toluene cracking by DFT calculations. The presence of Si elevated the E_{ad} on the Si co-doped CaO surface by 62.4%, and the enhanced toluene decomposition was attributed to the modification of the adsorption structure; thus, toluene decomposition on the Si co-doped CaO material surface was improved. Further analysis identified that -H and -OH radicals formed through steam decomposition served as primary reactive intermediates responsible for tar cracking, and dehydrogenation at the ortho position acted as the rate-determining step. Therefore, a powerful approach for unraveling these surface phenomena and electronic interactions at the atomic scale can be provided by DFT calculations, through which vital theoretical insights into the structure–reactivity relationships of CaO-based materials are expected to be obtained.

In this work, DFT investigations were carried out to clarify the fundamental mechanisms of sintering resistance and tar cracking over Ni/Ce co-doped CaO materials. To evaluate the sintering resistance mechanism at the atomic scale, the adsorption behavior of Ca_4O_4 clusters, which were used as representative structural units for CaO agglomeration, was systematically examined on the doped surfaces. Furthermore, toluene was employed as a typical model compound for primary tar during steam gasification of biomass, and adsorption geometries, activation energies, and detailed bond cleavage pathways on the material surfaces were determined. The partial density of states (PDOS), charge transfer, activation barriers, and the intrinsic synergistic role of Ni and Ce doping were revealed, and essential theoretical guidance was provided for the rational design of highly robust and active CaO-based materials for H_2 production from steam gasification of biomass.

Computation

Methods

All DFT investigations of sintering resistance and tar decomposition on Ni- and Ce-doped CaO surfaces were carried out with the DMol^3 code[33,34]. Geometry optimizations and transition state (TS) searches were conducted using the spin-unrestricted generalized gradient approximation (GGA) with the Perdew–Burke–Ernzerhof (PBE) functional for exchange-correlation treatment. A 2 × 2 × 1 Monkhorst-Pack k-point grid was generated and adopted for all structural models. Convergence criteria for energy, force, and displacement were set to 10^{-5} Ha, 0.002 Ha/Å, and 0.005 Å, respectively. The self-consistent field (SCF) iteration was deemed converged when the tolerance reached 10^{-6} Ha. The DFT semi-core pseudopotential approach was employed for core electron treatment, and the double numerical plus polarization (DNP) basis set of v4.4 was adopted. Multipolar expansion was carried out using the hexadecapole angular momentum function. To facilitate SCF convergence, charge and spin density mixing parameters were assigned values of 0.2 and 0.5, respectively. A density preconditioner with q_0 of 4.0 a_0^{-1} was used. The Fermi thermal smearing at 0.005 Ha was applied to enhance SCF convergence while balancing computational efficiency and accuracy. The complete LST/QST protocol was employed for TS search. To guarantee the reliability of transition state configurations, the TS search, optimization, and confirmation calculations were conducted.

Models and energies definitions

The (0 0 1) low Miller index plane of CaO was selected as the representative surface because this facet has been proven to exhibit low surface energy[35,36]. The 2 × 2 periodic supercell was deemed adequate to the essential characteristics of CaO-based surfaces for H_2S adsorption[37], water-gas-shift[38], and H_2O adsorption[39]. Accordingly, a slab model of CaO (0 0 1) surface consisting of four

atomic layers within a 2 × 2 periodic supercell was constructed, as illustrated in Supplementary Fig. S1a. A vacuum layer of 20 Å was inserted perpendicular to the CaO (0 0 1) surface to avoid interactions between periodic images. After one Ca atom in the top layer is substituted by a Ni or Ce atom, the Ni- or Ce-doped CaO surfaces are obtained, as exhibited in Supplementary Fig. S1b, S1c, which are denoted as Ni-CaO and Ce-CaO, respectively. Besides, the Ni and Ce-co-doped CaO surface is built with two Ca atoms substituted by Ni and Ce atoms, respectively, denoted as Ni-Ce-CaO. The two lowermost atomic layers of the periodic slab were fixed in both Cartesian and fractional coordinates, while the rest of the slab model, including the top two layers and all adsorbates, was treated as relaxed. Prior to being placed on the CaO surface, the isolated molecules and clusters, including the Ca_4O_4, toluene, and reaction intermediates, were optimized individually within a 20 Å × 20 Å × 20 Å cubic cell to eliminate spurious periodic effects. Partial Hessian vibrational frequency computations were performed for all adsorption and TS configurations[40]. To ensure the robustness of the optimized structures, the absence of imaginary frequencies was verified for all relaxed adsorption configurations, whereas each TS configuration was confirmed to possess only one imaginary frequency, and the vibrational mode was aligned with the reaction coordinate.

The adsorption energy (E_{ad}) served as a quantitative indication of the thermodynamic favorability of each adsorption configuration. A more negative E_{ad} value corresponds to greater thermodynamic stability and a higher tendency to form. E_{ad} was calculated according to Eq. (2):

$$E_{ad} = E_{sys} - E_{adsorbate} - E_{surface} \quad (2)$$

where E_{sys} denotes the total energy of the adsorption system, eV; $E_{adsorbate}$ refers to the energy of the isolated adsorbate, eV; and $E_{surface}$ represents the energy of the clean surface, eV. The activation barrier (E_a) for every elementary step was evaluated via Eq. (3)[41]:

$$E_a = E_{TS} - E_R \quad (3)$$

where E_{TS} and E_R denote the energies of the transition state and the reactant, respectively, in eV. The larger E_a corresponds to the kinetically less favorable elementary step. The formation energy (E_{form}) was applied to evaluate the thermodynamic feasibility of generating the doped surface configurations. The chemical potentials of the relevant elements (μ_e) were first derived from Eq. (4):

$$\mu = E_{sim}/n \quad (4)$$

where μ represents the chemical potential of a given element, eV; E_{sim} is the total energy of the most stable elemental substance, eV. n denotes the number of atoms in the simple substance or conventional cell. The formation energies of the doped configurations were determined from Eq. (5):

$$E_{form} = E_{sys} - E_{O_v\text{-}CaO} + \mu_O - \mu_e \quad (5)$$

where $E_{Ov\text{-}CaO}$ corresponds to the energy of the surface bearing one oxygen vacancy in the top layer, eV; μ_O and μ_e are the chemical potentials of oxygen and the dopant element, respectively, eV.

Results and discussion

Energy and electronic characteristics of Ni- and Ce-doped CaO surfaces

Supplementary Fig. S1a–S1d shows that the Ni- or Ce-doped CaO surfaces appear similar in structure to those of the CaO surface, and the positions of the Ca and O atoms remain stable after doping. E_{form} of the three doped CaO surfaces were calculated according to Eq. (5) and are found to be 2.99, −1.90, and 0.54 eV, respectively. The positive E_{form} of Ni-CaO indicates its instability, and the Ni atom exhibits obvious inward relaxation toward the sublayers. In view of Ce-CaO and Ni-Ce-CaO, the negative E_{form} suggests facile formation and enhanced stability of these surfaces. Therefore, Ce doping improves the stability of the corresponding surfaces. Fig. 1a–d depict band structure patterns of the four surfaces. The band gap of CaO is calculated to be 3.49 eV, which is lower than the experimental value. This deviation results from the well-known tendency of the GGA functional to underestimate band gaps in crystalline materials. In the presence of Ni, the band gap is decreased to 3.05 eV, owing to the slight upward shift of the valence band, whereas the conduction band of the Ni-CaO surface changes little. The Ce-CaO surface possesses an ultra-narrow band gap of 0.02 eV, due to the formation of a new energy level near the Fermi Level. Additionally, the Ni-Ce-CaO surface also achieves a narrow band gap of 0.08 eV, which is between those of the two aforementioned surfaces. Based on the observed band gap narrowing, a semiconductor-to-conductor-like transition can be inferred for the Ni- and Ce-doped CaO surfaces. Consequently, electronic transport from the highest occupied molecular orbital to the lowest unoccupied molecular orbital becomes considerably more facile on these surfaces, which is expected to promote their reactivity.

The electron density difference was analyzed to investigate electron transfer in the pristine CaO surface and the doped surfaces, and the results are presented in Fig. 2, where the red and blue contours denote the increase and decrease of electron density, respectively. The pristine CaO surface exhibits a homogeneous electron distribution, and the electron density of the Ca and O atoms remains largely unchanged in the absence of dopants. Moreover, a greater amount of negative charge accumulates around the O atoms, which agrees well with their high electronegativity. For the Ni-CaO surface, the charge distribution in the top layer is altered. The charge density of the oxygen atoms adjacent to the Ni atom decreases from −1.054 to −1.130 e, whereas the charge density of the Ni and Ca atoms increases, indicating the Ni atom achieves a high effect on the neighboring O atoms. The Ce-CaO surface exhibits similar electronic characteristics, although the negative charge of the Ce atom is 0.34 e lower than that of the Ni atom, owing to differences in their initial charges. For the Ni-Ce-CaO surface, the electronic charge of the Ni atom decreases from 0.405 to −0.038 e, and abundant electrons are migrated to Ni atoms in the presence of Ce. This indicates obvious interaction between Ce and Ni species, which promotes reactivity. These results collectively indicate that the incorporation of Ni or Ce atoms disrupts the uniform electron distribution of the pristine CaO surface, leading to localized charge redistribution. In the Ni-CaO surface, the electron depletion around neighboring O atoms and the concurrent electron accumulation on Ni suggest a directional electron transfer from O to Ni. In the Ce-CaO surface, a redistribution pattern is noted, though the magnitude differs due to the distinct electronic properties of Ce. In the co-doped Ni-Ce-CaO surface, the presence of Ce species further enhances electron accumulation on Ni, implying collaborative electronic interaction of the two dopants. Therefore, Ni and Ce doping introduce electron imbalance on the CaO-based material surfaces and facilitate charge transfer between dopant atoms and both neighboring O atoms and adsorbate species, which is favorable for adsorption on these surfaces.

https://doi.org/10.48130/prkm-0026-0020

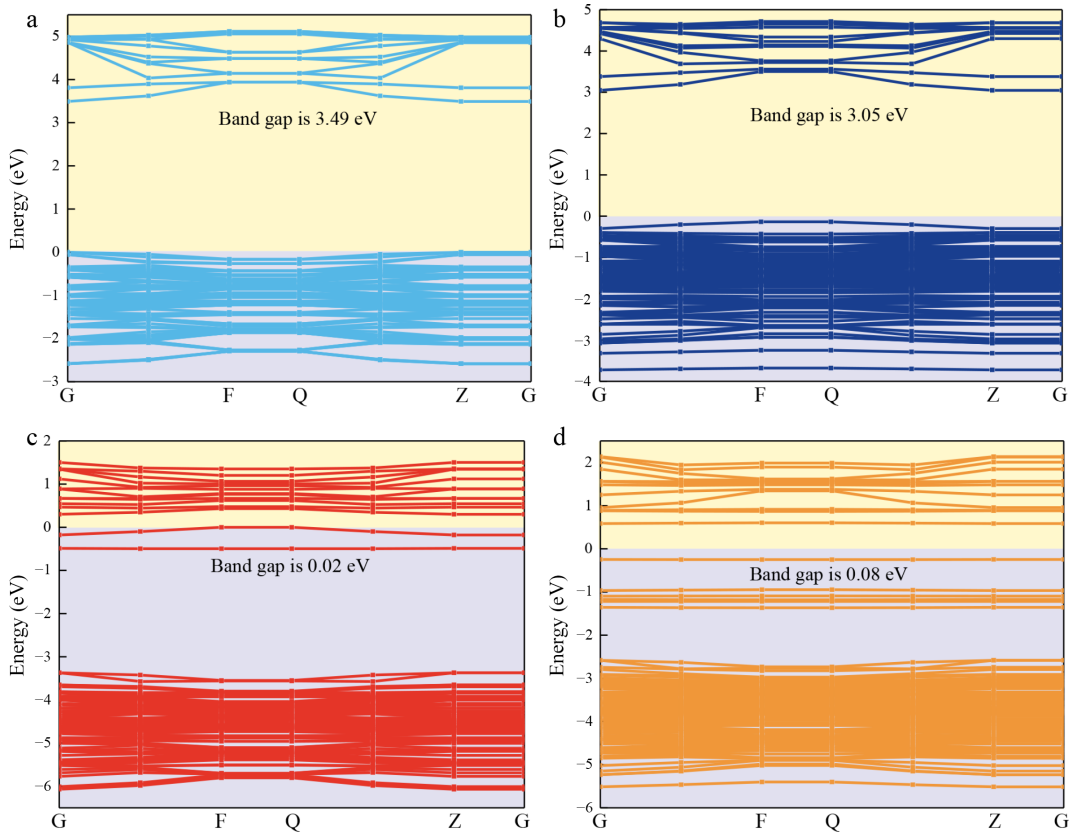

Fig. 1 Calculated band structure of (a) CaO, (b) Ni-CaO, (c) Ce-CaO, and (d) Ni-Ce-CaO surfaces.

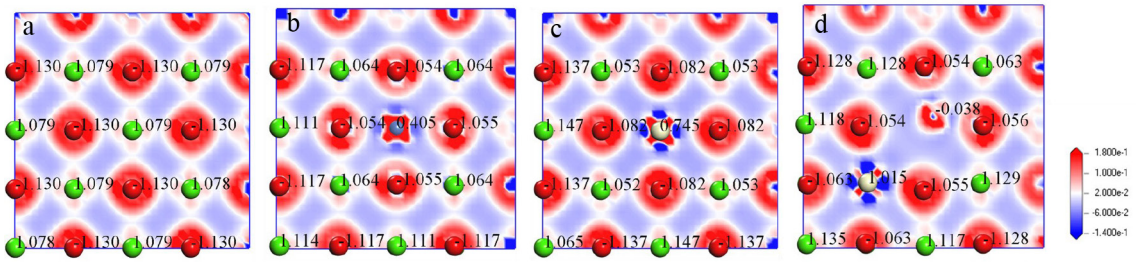

Fig. 2 Electron density difference and Mulliken charge population of (a) CaO, (b) Ni-CaO, (c) Ce-CaO, and (d) Ni-Ce-CaO surfaces.

Figure 3 displays the PDOS of several key atoms in the CaO, Ni-CaO, Ce-CaO, and Ni-Ce-CaO surfaces. In terms of the pristine CaO surface, the Ca atoms exhibit characteristic peaks at −18, −14, and −1 eV, which shift slightly toward decreased energy levels on the Ni-CaO surface, and the PDOS of the O atoms exhibit a similar trend. This indicates that the presence of Ni has a restricted effect on the surface stability, whereas characteristic peaks generated neighboring the Fermi level of the Ni-CaO surface lead to enhanced electron transition capability and reactivity. On the Ce-CaO surface, the introduction of Ce drives a pronounced downward shift of the characteristic peaks of the Ca and O atoms toward decreased energy levels, suggesting improved surface stability. Significant resonance peaks are observed between the Ce-d orbital and the O-p orbitals, indicating formation of a stable Ce–O bond, which may account for the enhanced stability of the Ce-CaO surface. Moreover, new energy levels involving the Ce d and f orbitals are introduced near the Fermi level, which indicates robust Ce-Ni interaction that further boosts the reactivity of CaO. With further introduction of a Ce atom to the Ni-CaO surface, its characteristic peaks shift to lower energy levels and generate a Ce–O bond, demonstrating the improved overall stability of the Ce-Ni-CaO. Similar to the Ce-CaO surface, new energy levels near the Fermi level are introduced with the Ni d and Ce f orbitals, and the intensity of these characteristic peaks is enhanced. This observation indicates an obvious interaction between Ce and Ni atoms, which further promotes the reactivity of CaO. Therefore, both Ni and Ce doping enhance the reactivity of CaO. The Ce–O bonds formed upon Ce doping provide greater stability. The differences in PDOS between Ni and Ce atoms arise from their distinct electronic structures and magnetic properties, resulting in different bonding modes among Ca, O, Ni, and Ce atoms on the doped configurations. The Ni-Ce-CaO surface simultaneously benefits from the improved stability provided by Ce doping and the enhanced reactivity induced by Ni doping, which facilitates the interaction between the surface and adsorbates and consequently achieves optimal adsorption performance.

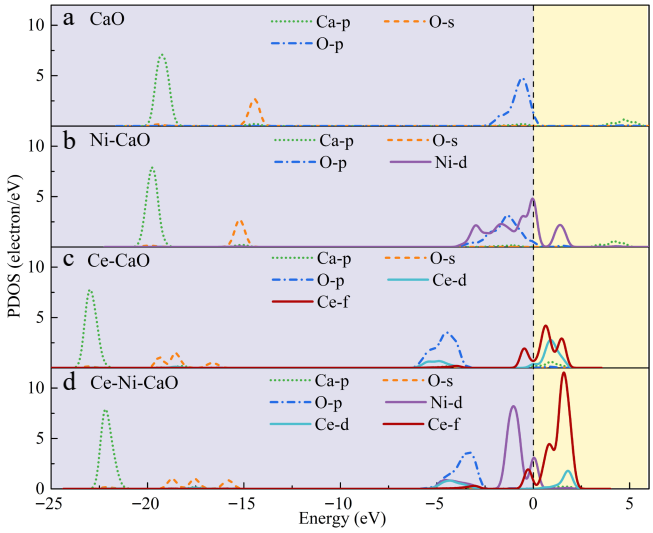

Fig. 3 PDOS of (a) CaO, (b) Ni-CaO, (c) Ce-CaO, and (d) Ni-Ce-CaO surfaces.

CO_2 molecule adsorption of Ni and Ce-doped CaO surfaces

Geometry optimizations for CO_2 adsorption were carried out on the CaO, Ni-CaO, Ce-CaO, and Ni-Ce-CaO surfaces. Since the O-top position has been generally regarded as appropriate for CO_2 capture on CaO, the optimized CO_2 molecule was initially placed on the O atoms of each CaO-based surface at a starting separation of 3 Å. It should be noted that symmetry and periodicity are significant to adsorption sites; thus, all O top sites on the CaO surface are equivalent. The substitution of a Ca atom by an Ni or Ce atom introduces charge redistribution due to the different valence electron configurations, as plotted in Fig. 2. The electron density of O atoms neighboring the doped atoms is significantly changed, compared with the far-away O atoms, which leads to a different coordination environment and CO_2 adsorption affinity of the O top sites. Therefore, the O atoms directly adjacent to, and far from, the doped atoms were selected as the typical sites for CO_2 adsorption. In this manner, two types of O top sites were selected for the Ni-CaO and Ce-CaO surfaces, namely those close to and far from the dopant atoms. Four distinct O top sites on the Ni-Ce-CaO surface were investigated.

Supplementary Fig. S2 displays the optimized configurations of the four surfaces following CO_2 adsorption, and the relevant adsorption energies are presented in Supplementary Table S1. Upon interaction, the separation between CO_2 and the surfaces decreases, the contraction of C–O bonds is observed, and the initially linear CO_2 molecule adopts a curved geometry. On the basis of the E_{ad} of CO_2 and the formation of a CO_3^{2-}-like structure, the direct chemisorption of CO_2 on these surfaces is confirmed. Both Ni and Ce doping enhance the CO_2 adsorption energy to varying degrees. For the Ni-CaO surface, E_{ad} of CO_2 at both adsorption sites is increased, whereas the Ce-CaO surface exhibits higher CO_2 E_{ad} only distant from the Ce atom. A similar trend is observed for the Ni-Ce-CaO surface. This behavior can be attributed to the altered electron distribution around the neighboring O atoms induced by the presence of doped Ni and Ce atoms, as discussed above based on the Mulliken charge population analysis. Both Ni and Ce doping enhance the CO_2 adsorption performance of CaO, though the overall improvements are relatively similar. This can be attributed to the intrinsic chemisorption of CO_2 on the CaO surface, which limits the extent to which the adsorption can be further increased. However, the coordination environment of the surface O sites can be modified by the localized charge redistribution on the doped CaO-based material surfaces. The introduction of Ni and Ce atoms leads to less negative Mulliken charges of the surface O atoms, indicating electron migration towards the doped atoms, as discussed in Fig. 2. The localized charge redistribution provides better conditions for CO_2 adsorption on specific O top sites. The preferential enhancement at specific O top sites further indicates that the charge redistribution is induced by the dopants, which may offer a rational basis for tailoring CaO-based materials with optimized CO_2 capture performance. Although the Ce-CaO surface exhibits excellent thermodynamic stability, it lacks the Ni active center that is essential for efficient catalytic tar cracking, and the objective of this study is to develop a robust dual-functional material. Therefore, the pristine CaO, Ni-CaO, and Ni-Ce-CaO surfaces were selected in the following investigations.

Ca_4O_4 cluster adsorption of Ni- and Ce-doped CaO surfaces

A Ca_4O_4 cluster was employed as a representative structural model to evaluate the sintering resistance of the CaO-based surfaces, and its optimized configurations and geometric parameters are demonstrated in Supplementary Fig. S3 and Supplementary Table S2, respectively. It can be observed that the optimized configuration of the Ca_4O_4 cluster exhibits a slightly distorted cube. A limited variation of Ca–O bond lengths is found, while the bond angles are distinct; the O–Ca–O bond angles are expanded, and the Ca–O–Ca bond angles are compressed, which results from the repulsion effects of Ca atoms. Figure 4 illustrates the Ca_4O_4 cluster adsorption configurations on CaO, Ni-CaO, and Ni-Ce-CaO surfaces. The adsorption energies of the Ca_4O_4 cluster on the pristine CaO, Ni-CaO, and Ni-Ce-CaO surfaces are calculated to be −2.72, −2.99, and −3.27 eV, respectively. Distinct Ca_4O_4 cluster adsorption configurations and energies are obtained on different surfaces, indicating varying strength of cluster–surface interaction, due to the elevated E_{ad} of the Ca_4O_4 cluster in the presence of doped atoms. On pristine CaO, the original arrangement of the Ca_4O_4 cluster is maintained, and no significant structural displacement is observed. In contrast, noticeable structural deformation of the Ca_4O_4 cluster is induced on both the Ni-CaO and Ni-Ce-CaO surfaces, suggesting that effects on the overall structural stability of the system are exerted by the Ni and Ce doping. For the Ni-CaO surface, the upward shift of the Ni atom is observed after Ca_4O_4 adsorption, and strong interaction with the O atom in the Ca_4O_4 cluster and the formation of a Ni–O bond are demonstrated. This displacement reveals that the Ni atom is structurally unstable and is prone to migrate, further indicating that the high-temperature sintering of CaO is aggravated by Ni doping[27]. Such instability can be associated with the weak interaction between Ni and the CaO lattice, as demonstrated by the positive formation energy discussed earlier. For the Ni-Ce-CaO surface, an obvious displacement of the Ca_4O_4 cluster is achieved upon adsorption, and greater displacement is associated with the stronger interfacial interaction, in view of the high Ca_4O_4 cluster adsorption energy of −3.27 eV. Besides, no obvious structural change is observed for the Ni-Ce-CaO surface; thus, the incorporation of Ce can not only strengthen interaction with the Ca_4O_4 cluster but also enhance the lattice integrity of the surface. Therefore, the structural stability of the substrate is enhanced by Ce doping. The adsorption capacity toward the Ca_4O_4 cluster is enhanced on doped CaO-based material surfaces relative to the pristine surface. Among the three surfaces, the highest adsorption energy is

https://doi.org/10.48130/prkm-0026-0020

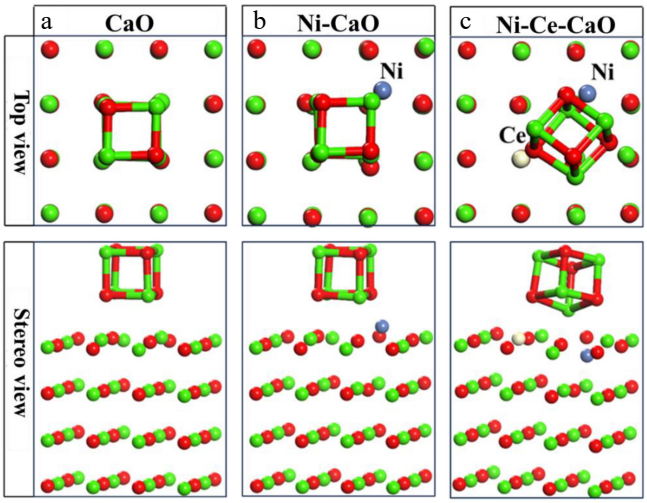

Fig. 4 Adsorption configurations of the Ca_4O_4 cluster on (a) CaO, (b) Ni-CaO, and (c) Ni-Ce-CaO surfaces.

achieved by the Ni-Ce-CaO surface, which is 20% higher than that of the pristine CaO surface; thus, its superior structural stability and sintering resistance are demonstrated. The adsorption energy is ranked in the order of Ni-Ce-CaO, Ni-CaO, and CaO. The results indicate that Ni and Ce co-doping plays a crucial role in enhancing the interfacial interaction with the Ca_4O_4 cluster, which is expected to suppress sintering and extend the operational durability of doped materials.

Figure 5a–c presents the electron density difference maps obtained for Ca_4O_4 cluster adsorption on pristine CaO, Ni-CaO, and Ni-Ce-CaO surfaces. Since the doped Ni and Ce atoms are located along the diagonal of the CaO surface, the selected cross-section can express the electronic characteristics of both the dopant atoms and the adsorbed Ca_4O_4 cluster simultaneously. By comparison with the electron density difference maps of the corresponding surfaces prior to adsorption shown in Fig. 2, it can be observed that adsorption of the Ca_4O_4 cluster leads to electron transfer, which leads to charge density redistribution. For the pristine CaO surface, only weak electron transfer is observed, which suggests limited interaction by weak chemisorption or van der Waals forces. Upon Ni doping, distinct electron transfer is observed between the Ca_4O_4 cluster and the Ni-CaO surface. A shift of the Ni atom toward the Ca_4O_4 cluster is noted, accompanied by the formation of a Ni–O bond, indicating that the reactivity of the CaO surface is enhanced by Ni doping, though the structure of the Ni-CaO surface remains unstable. The instability may be correlated with its positive formation energy of the Ni-CaO surface; thus, the surface is more susceptible to structural rearrangement in the presence of the adsorbate. In contrast, a significant redistribution of electron density is observed on the Ni-Ce-CaO surface. Moreover, the interaction between Ce and Ni atoms results in downward displacement of the Ni atom, which may be associated with the suppression of Ni agglomeration by Ce atoms. Accordingly, different electronic states are introduced by Ce and Ni doping, leading to distinct patterns of electron density variation on the two doped surfaces, which ultimately influence the electronic structure and catalytic performance of the doped surfaces.

Figure 6 exhibits the PDOS of various key atoms after Ca_4O_4 cluster adsorption. As shown in Fig. 6a, negligible weak resonance peaks are generated between Ca and O atoms on the CaO surface with the O and Ca atoms of the cluster, because of the weak interaction between the CaO surface and the Ca_4O_4 cluster. Upon Ni doping, as presented in Fig. 6b, distinct electron transfer and orbital overlap occur between the Ni-d orbitals and O-p orbitals in the cluster. This indicates that a chemical reaction occurs with Ni atoms in the substrate and the Ca_4O_4 cluster to form a Ni–O bond. Ni doping introduces new energy levels neighboring the Fermi level; thus, the charge distribution of neighboring O atoms is altered. For the Ni-Ce-CaO surface as shown in Fig. 6c, the overall energy levels of the Ni-CaO surface and the Ca_4O_4 cluster are shifted toward lower energy levels. Therefore, the adsorption of the Ca_4O_4 cluster is enhanced, and the adsorption behavior of the Ca_4O_4 cluster is closely related to the sintering resistance of the catalyst. The Ce-p orbitals are hybridized simultaneously with both surface and cluster O orbitals to form a CeO_2 structure, which may explain why the stability of the Ni-CaO surface is improved by Ce doping. Furthermore, additional characteristic peaks are introduced near the Fermi level in the Ni-Ce-CaO surface by Ce doping, and the reactivity is further elevated. Accordingly, the catalytic performance is enhanced by Ni atoms mainly through the introduction of new characteristic peaks near the Fermi level and the amplification of charge imbalance between O and the Ni atoms. The overall stability is improved by Ce atoms primarily via the hybridization between Ce orbitals and O orbitals, which results in a stable CeO_2-like structure. The Ni-Ce-CaO surface shown in Fig. 6c not only benefits from the strong catalytic activity associated with NiO but also exhibits the high sintering resistance characteristics of CeO_2. The incorporation of the Ce atom introduces localized lattice expansion, which significantly increases the diffusion barrier for Ni atoms. The doped Ce atom also acts as a strong electron donor, and the localized charge redistribution is achieved to enrich the electron density of adjacent O atoms; thus, the strength of Ni–O bonds can be enhanced. The results suggest that the electronic characteristics of the original pristine CaO surface are improved in a complementary manner by the synergistic incorporation of Ni and Ce, thereby enabling catalytic reactivity with structural stability to be achieved simultaneously.

Cyclic CO_2 capture performances of Ni- and Ce-doped CaO materials

Cyclic tests have been carried out to determine the CO_2 capture performance and sintering resistance of the multiple Ni- and Ce-doped CaO materials, according to the Experiment section in Supplementary File 1. As shown in Supplementary Fig. S4a, pristine CaO exhibits a drastic decrease in CO_2 absorption capacity from 0.729 to 0.292 g/g during 20 cycles, indicating that severe sintering of CaO grains occurs over the cycles. In the presence of 5 wt% Ni, the CaO content in the materials is lower than that of pristine CaO, resulting in lower initial CO_2 capture capacities. However, after two cycles, the CO_2 capture capacity is improved compared with pristine CaO, indicating that the CO_2 absorption activity of CaO can

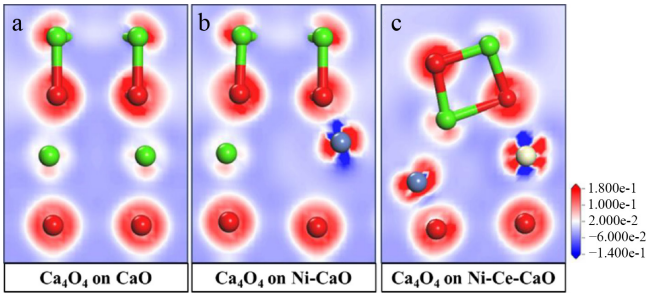

Fig. 5 Electron density difference of Ca_4O_4 cluster adsorption on (a) CaO, (b) Ni-CaO, and (c) Ni-Ce-CaO surfaces.

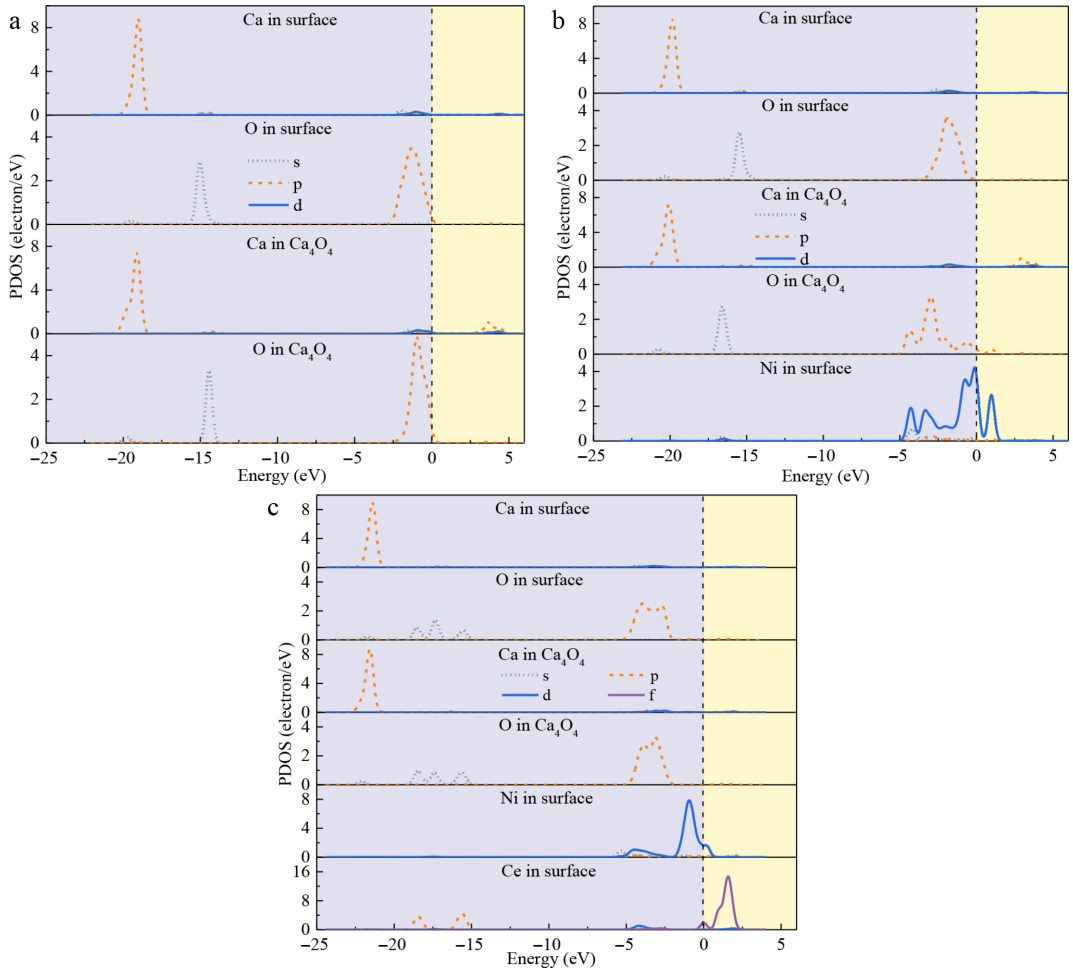

Fig. 6 PDOS of Ca_4O_4 cluster adsorption on (a) CaO, (b) Ni-CaO, and (c) Ni-Ce-CaO surfaces.

be improved with Ni doping, and more CO_2 is included despite the lower CaO content. After 20 cycles, a 57.7% reduction in CO_2 absorption capacity is exhibited, while the deactivation trend is similar to that of pristine CaO. This phenomenon suggests that the sintering resistance performance of CaO is not improved by Ni doping, and severe sintering of the Ni-CaO materials still occurs with an increasing number of cycles[42]. As the Ni doping content is improved to 10 wt% and 20 wt%, further decreases in CO_2 absorption capacities in the initial two cycles can be observed. Although the CO_2 capture trend of Ni_{20}-CaO was identical to that of Ni_{10}-CaO, the CaO content was severely reduced by excessive Ni. In the presence of Ce, during 20 cycles, CO_2 absorption capacity decreases by only 27.7% for Ce_5-CaO, and a similar attenuation trend can be observed with $Ni_{10}Ce_5$-CaO, indicating that the cyclic stability can also be enhanced by Ce incorporation compared with Ni doping. Further increases in Ce loading content improve the sintering resistance of Ce-CaO material, while insufficient CaO content in the materials is also caused by excessive Ce. Thus, the optimal cyclic CO_2 capture performance was exhibited by Ce_{10}-CaO, with a CO_2 absorption capacity of 0.663 g/g in the 1st cycle, which decreased by only 15.7% during the cycles. Cyclic CO_2 capture performances of Ni-Ce-CaO materials are highly similar to those of Ce-CaO, while the effective CaO content of the Ni-Ce-CaO material is reduced, and a lower CO_2 absorption capacity is obtained. $Ni_{10}Ce_{10}$-CaO achieves a CO_2 absorption capacity of 0.523 g/g after 20 cycles, which is 79% higher than that of pristine CaO. Carbonation conversion in Supplementary Fig. S4b exhibits a similar trend to CO_2 absorption capacity, and the Ni-Ce-CaO materials achieve higher X_N within 20 cycles. This phenomenon results from a decreased CaO content in the materials, due to the presence of doped Ni and Ce. The low cyclic deactivation extent of Ni-Ce-CaO confirms the sintering resistance mechanism by DFT calculation results. Because the Ce doping enhances the adsorption of the Ca_4O_4 cluster, the diffusion and transportation of lattice Ca and O atoms under elevated temperature during the cycles are inhibited by kinetics. The improvement of the diffusion energy barrier is reflected by the stable X_N curve during 20 cycles; thus, the agreement between the intrinsic mechanism and deactivation kinetics is achieved.

Therefore, the high initial capture capacity of Ni-doped CaO is consistent with DFT calculation results, which show that Ni doping increases the CO_2 adsorption energy, and electron transfer from Ni to surface O atoms strengthens basicity and stabilizes the adsorbed CO_2. However, Ni doping cannot directly increase the diffusion barriers of lattice Ca^{2+} and O^{2-} ions. High-temperature stability of Ni-CaO remains hindered, and severe sintering and rapid CO_2 absorption capacity decay are observed. The high cyclic stability of CaO-based materials in the presence of Ce is well-supported by DFT calculations. Ce doping increases the migration barriers of the Ca_4O_4 cluster; thus, the grain growth at high temperatures can be inhibited. This result is in agreement with the experimental observation of enhanced cyclic stability of materials in the presence of Ce doping, despite the dilution of the effective CaO content by excessive Ce.

https://doi.org/10.48130/prkm-0026-0020

Toluene adsorption of Ni- and Ce-doped CaO surfaces

Supplementary Fig. S5 exhibits the most stable configuration of toluene adsorption on CaO, Ni-CaO, and Ni-Ce-CaO surfaces. It can be observed that the molecule of toluene almost remains unchanged after adsorption on the surfaces, in which the C–C and C–H bond cleavage is absent. Besides, no significant interactions between the molecule and the surfaces can be inferred, and the E_{ad} of the toluene molecule are −0.27, −0.54, and −0.54 eV on CaO, Ni-CaO, and Ni-Ce-CaO, respectively, demonstrating the occurrence of physical adsorption. Therefore, an unstable toluene adsorption configuration on the pristine CaO surface can be inferred, which is prone to desorb from the surface, inhibiting the following reaction. Upon Ni and Ce doping, the adsorption energy of toluene is nearly twice that of the pristine CaO surface, which can facilitate the tar cracking reaction. The enhanced physical adsorption induced by the dopants may extend the residence time of toluene on the surfaces, and the subsequent bond activation and ultimately cleavage during the toluene cracking process can be promoted.

Figure 7 depicts the PDOS of toluene adsorption on Ni-CaO and Ni-Ce-CaO surfaces. As observed from the PDOS patterns, toluene adsorption exerts a negligible effect on the PDOS of the Ni atom, and no electron transfer between the Ni atom and the toluene molecule is detected. It is thus confirmed that toluene adsorption on CaO-based material surfaces is classified as physical adsorption. Upon Ce doping, the overall energy levels of Ni atoms are shifted leftward, which demonstrates that the structural stability is improved by the introduction of Ce. In general, higher characteristic peak intensity facilitates electron localization. The peak intensity of Ni atoms in the Ni-CaO surface is distributed in the range from 0 to 5 electrons/eV, whereas this value is increased to 8 electrons/eV after Ce doping. Such enhancement demonstrates that the Ni atom in the Ni-Ce-CaO surface is more readily able to form chemical bonds with other atoms. Consequently, the electronic structure of the Ni atom is modulated by Ce doping, and both the surface electronic activity and the structural stability of the surface are enhanced. The dual improvements may provide favorable conditions for the subsequent catalytic activation of the adsorbed toluene, and C–H and C–C bond cleavage during the cracking process can be promoted.

Toluene cracking on Ni- and Ce-doped CaO surfaces

The toluene molecule cracking pathway is schematically presented in Supplementary Fig. S6. The most appropriate cracking path of toluene is initiated by the elimination of three H atoms from the methyl group. After the complete dehydrogenation of the methyl group, the C–H bonds on the benzene ring can be activated. Subsequently, one H atom at the ortho position relative to the methyl group is desorbed, and the ring-opening reaction is finally triggered to generate small-molecule hydrocarbons. Therefore, the activation energies of the elementary reactions along the toluene cracking process are calculated, and the results are shown in Fig. 8. To compare the effect of catalyst doping on the activation barrier, the energy of the initial structure of every elementary reaction is unified at the same horizontal coordinate of 0 eV.

As observed in Fig. 8a–c and e, the activation barrier required for toluene cracking on the pristine CaO surface is found to be the largest, which is attributed to negligible interaction between toluene with CaO surface, which is insufficient to stabilize the transition states involved in bond activation and cleavage. On the pristine CaO surface, long residence time of generated intermediates, including benzyl or phenyl fragments, could be achieved after toluene cracking; thus, side reactions are prone to be triggered, and further condensation of the intermediates could result in carbon deposition and deactivation of the material. The slight decrease in the activation barrier is caused by Ni doping, and further reduction is achieved in the presence of Ce, which demonstrates collaborative enhancement of Ni and Ce on tar cracking. It should be noted that for the dehydrogenation reaction on the benzene ring shown in Fig. 8d, the activation barrier on the pristine CaO surface is the

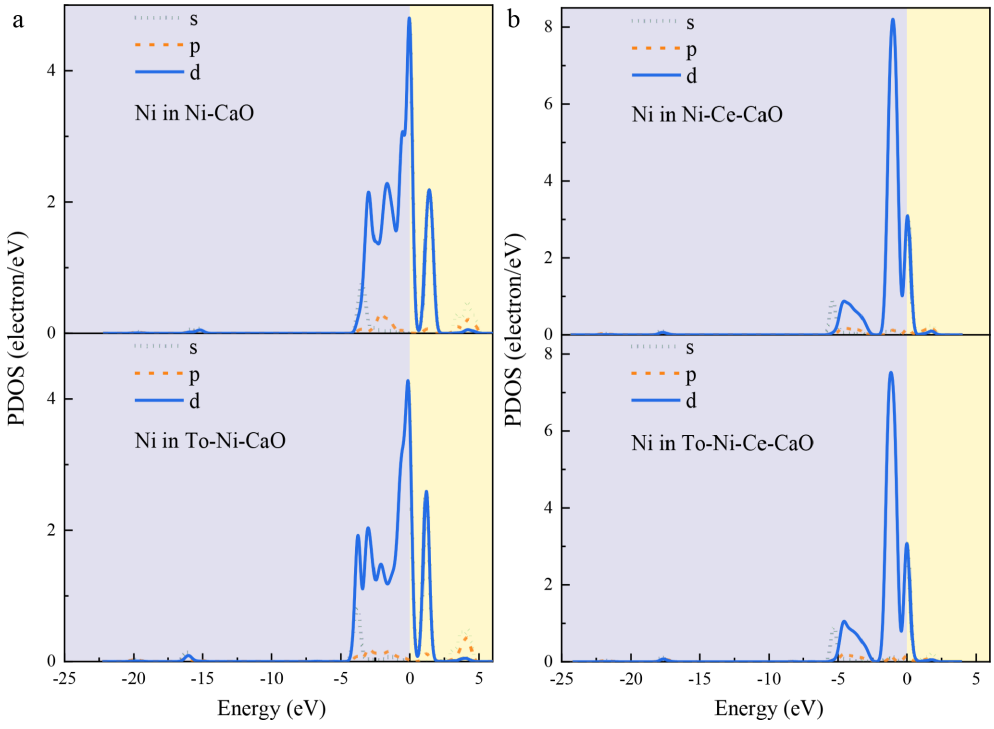

Fig. 7 PDOS of toluene adsorption on (a) Ni-CaO, and (b) Ni-Ce-CaO surfaces.

lowest among the three surfaces, with a value of 3.08 eV. The activation barrier is greatly increased to 4.94 eV by Ni introduction, which is slightly reduced to 4.28 eV by the further doping of Ce. This variation may be attributed to the selective catalysis of Ni toward toluene, while the adsorption configuration is altered so that the ortho C–H bond on the benzene ring becomes less accessible; thus, a higher activation energy is required. However, for the overall toluene cracking pathway, the elementary reaction with the highest energy barrier is regarded as the rate-determining step, and the formation of products is governed by the activation barrier of this step. The presence of Ni and Ce could introduce active d or f orbital electrons near the Fermi level as discussed above, and the cleavage of C–C and C–H bonds can be enhanced by the charge injection. This kinetic charge transfer stabilizes the TS configuration, and the energy required for TS generation is reduced. Although the activation barrier of the fourth dehydrogenation step is increased by Ni and Ce doping, the ring-opening reaction in Fig. 8e is the rate-determining step in view of the entire pathway, as it possesses the greatest energetic demand. The activation barrier of this rate-determining step is reduced from 8 to 6.3 and 5.3 eV by Ni and Ni/Ce co-doping, respectively, indicating that the combination doping facilitates the C–C bond cleavage necessary for ring opening effectively. According to the intrinsic kinetic relationship of Arrhenius Law, the decrease in activation barrier can lead to exponential improvement of the reaction rate constant. Under the realistic high temperatures during biomass gasification, the activation barrier of ring-opening on the Ni-Ce-CaO surface can be reduced, indicating that the intrinsic reaction rate of toluene cracking would be

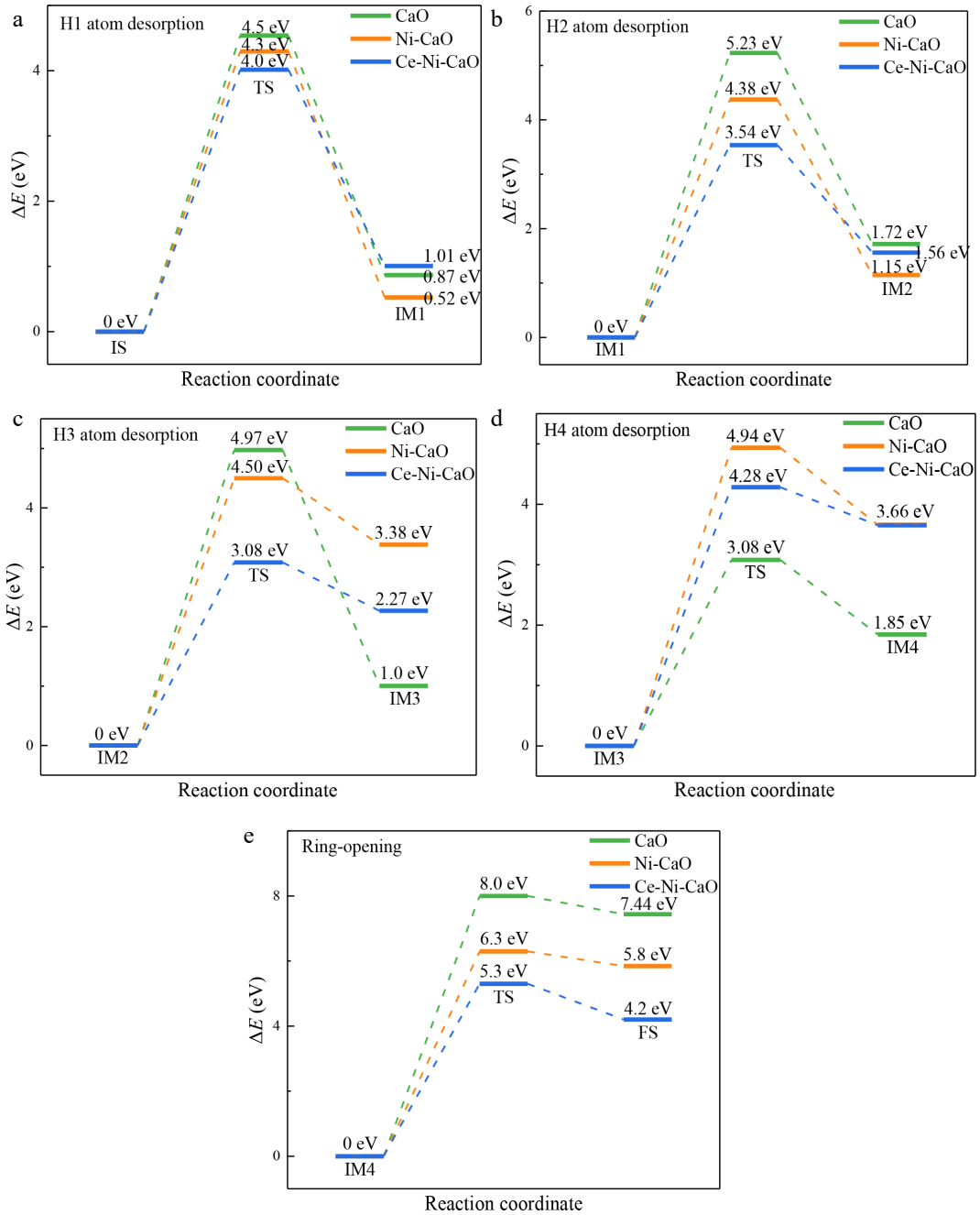

Fig. 8 Relevant energies of toluene cracking reaction on CaO, Ni-CaO, and Ni-Ce-CaO surfaces: (a) H1 atom desorption, (b) H2 atom desorption, (c) H3 atom desorption, (d) H4 atom desorption, and (e) ring-opening.

https://doi.org/10.48130/prkm-0026-0020

improved significantly compared with that on pristine CaO. Therefore, the decomposition of toluene is promoted by Ni and Ce doping. The most appropriate catalytic effect on toluene cracking is exhibited by the Ni-Ce-CaO surface, and co-doping is more favorable for the formation of small-molecule hydrocarbons and H_2. Such enhancement results from the modulation of the energetic profile of the rate-determining step, which ultimately accelerates the tar reforming process.

Conclusions

In this work, the enhanced cyclic stability of Ni- and Ce-doped CaO-based materials was revealed with sintering resistance and catalytic tar cracking performance by DFT calculations, and the energetic and electronic characteristics of Ni- and Ce-doped CaO surfaces, together with their adsorption and catalytic behaviors, were systematically investigated. The formation energy calculations and electronic structure analysis demonstrate that though Ni doping introduces reactive electronic states near the Fermi level and reduces the band gap, it leads to structural instability, while negative formation energies are obtained for the Ce-doped CaO surface, and stable Ce–O bonds are formed through the hybridization of Ce 4d and O 1s orbitals, by which the overall surface stability is significantly improved. On the Ni-Ce-CaO surface, the advantages of both dopants are integrated. New electronic states are introduced near the Fermi level by Ni 3d and Ce 4f orbitals, and the lattice is stabilized by Ce–O bonds, and the agglomeration of Ni atoms is suppressed by Ce. This synergistic effect is presented by the strongest interaction between the surface and the Ca_4O_4 cluster, the most negative adsorption energy, and the most pronounced sintering resistance. For the catalytic cracking of toluene, the ring-opening step is identified as the rate-determining step. The activation barrier of this step is reduced from 8.0 eV on pristine CaO to 5.3 eV on the Ni-Ce-CaO surface, and the co-doped surface consequently exhibits the optimal catalytic performance; thus, the formation of small-molecule hydrocarbons and H_2 can be facilitated. Therefore, it can be concluded that a rational balance between reactivity and stability is achieved by the synergistic introduction of Ni and Ce, and the Ni-Ce-CaO surface holds considerable promise for high-temperature applications involving CO_2 capture, sintering resistance, and tar cracking.

Author contributions

The authors confirm their contribution to the paper as follows: writing – original draft: Yan X, Ding B, Duan C; investigation: Yan X, Duan C; visualization: Yan X, Ding B, Zhou X; funding acquisition: Liu F, Chu H; writing – review and editing: Liu F, Deng W, Chu H; supervision: Chu H. All authors reviewed the results and approved the final version of the manuscript.

Data availability

The datasets generated and/or analyzed in the current study are available from the corresponding author upon reasonable request.

Acknowledgments

This work was supported by the National Natural Science Foundation of China (No. 52206226) and the Open Project of State Key Laboratory of Continental Shale Oil.

Conflict of interest

The authors declare that they have no known competing financial interests or personal relationships that could have appeared to influence the work reported in this paper.

Supplementary information accompanies this paper online at: https://doi.org/10.48130/prkm-0026-0020.

Dates

Received 12 June 2026; Revised 8 July 2026; Accepted 14 July 2026; Published online 11 September 2026

References

[1] Peng M, Ge Y, Gao R, Yang J, Li A, et al. 2025. Thermal catalytic reforming for hydrogen production with zero CO_2 emission. *Science* 387:769–775

[2] IPCC. 2023. *Climate Change 2023: Synthesis Report. Contribution of Working Groups I, II and III to the Sixth Assessment Report of the Intergovernmental Panel on Climate Change*. Core Writing Team, H. Lee and J. Romero (eds.). Geneva, Switzerland: IPCC. 184 pp doi: 10.59327/IPCC/AR6-9789291691647

[3] Chong CT, Zhang H, Goh BHH, Ahmed S, Jalili AR, et al. 2026. Development of cobalt-based perovskite catalysts for hydrogen production via ammonia decomposition. *Progress in Reaction Kinetics and Mechanism* 51:e010

[4] Oni BA. 2025. A review on electrochemical water splitting electrocatalysts for green H_2 production: unveiling the fundamentals and recent advances. *Langmuir* 41:10742–10767

[5] Zhang S, Liang D, Li X, Fan Y, Huang H, et al. 2026. Study on the mechanism of hydrogen production by catalytic pyrolysis of bagasse over CaO/Na_2CO_3. *Progress in Reaction Kinetics and Mechanism* 51:e002

[6] Yuan C, Zhu L, Wu S, Jiang L, Xu K, et al. 2026. In situ separable and stable Ca-based bifunctional pellets for hydrogen-rich syngas production via sorption-enhanced steam gasification of biomass. *Applied Catalysis B: Environment and Energy* 386:126392

[7] Boon J. 2023. Sorption-enhanced reactions as enablers for CO_2 capture and utilisation. *Current Opinion in Chemical Engineering* 40:100919

[8] Sun R, Shen H, Lv X, Wang Y, Hu T. 2024. Solution combustion synthesis of MgO-stabilized CaO sorbents using polyethylene glycol as fuel and dispersant. *RSC Advances* 14:1741–1749

[9] Capa A, Yan Y, Rubiera F, Pevida C, Gil MV, et al. 2023. Process simulations of high-purity and renewable clean H_2 production by sorption enhanced steam reforming of biogas. *ACS Sustainable Chemistry & Engineering* 11:4759–4775

[10] Fang Y, Li Y, Zhang Y, Wang Y, Han K, et al. 2025. Self-acceleration effect of Mn/Ce-modified carbide slag in CO_2 absorption for $CaO/CaCO_3$ energy storage. *Separation and Purification Technology* 357:130153

[11] Sun J, Li K, Xiong Y, Li X, Zhang X, et al. 2025. Microtubule-structured, dolomite-derived CO_2 sorbents synthesized by impregnated layer solution combustion for direct solar-driven calcium looping. *Separation and Purification Technology* 354:128980

[12] Masoudi Soltani S, Lahiri A, Bahzad H, Clough P, et al. 2021. Sorption-enhanced steam methane reforming for combined CO_2 capture and hydrogen production: a state-of-the-art review. *Carbon Capture Science & Technology* 1:100003

[13] Han L, Zhang Y, Lin K, Jia X, Zhang H, et al. 2017. Developing a novel CaO-based sorbent for promoted CO_2 capture and tar reduction. *Energy & Fuels* 31:5306–5317

[14] Quan C, Gao N, Wang H, Sun H, Wu C, et al. 2019. Ethanol steam reforming on Ni/CaO catalysts for coproduction of hydrogen and carbon nanotubes. *International Journal of Energy Research* 43:1255–1271

[15] Wang G, Guo Y, Yu J, Liu F, Sun J, et al. 2022. Ni-CaO dual function materials prepared by different synthetic modes for integrated CO_2 capture and conversion. *Chemical Engineering Journal* 428:132110

[16] Sun S, Zhang C, Wang Y, Zhao X, Sun H, et al. 2023. CO_2 capture from H_2O and O_2 containing flue gas integrating with dry reforming methane using Ni-doping CaO dual functional materials. *Chemical Engineering Journal* 468:143712

[17] Irfan M, Li A, Zhang L, Ji G, Gao Y, et al. 2021. Hydrogen-rich syngas from wet municipal solid waste gasification using Ni/Waste marble powder catalyst promoted by transition metals. *Waste Management* 132:96–104

[18] Guo D, Qi Z, Fu Z, Lv Z, Kang L, et al. 2025. Synergistic catalysis of Cu_xFe_y/CeO_2 bimetallic catalysts for oxidative dehydrogenation of C_2H_6 with CO_2. *Chemical Engineering Journal* 522:167157

[19] Esch F, Fabris S, Zhou L, Montini T, Africh C, et al. 2005. Electron localization determines defect formation on ceria substrates. *Science* 309:752–755

[20] Guo H, Feng J, Zhao Y, Wang S, Ma X. 2017. Effect of micro-structure and oxygen vacancy on the stability of (Zr-Ce)-additive CaO-based sorbent in CO_2 adsorption. *Journal of CO_2 Utilization* 19:165–176

[21] Wang S, Fan S, Fan L, Zhao Y, Ma X. 2015. Effect of cerium oxide doping on the performance of CaO-based sorbents during calcium looping cycles. *Environmental Science & Technology* 49:5021–5027

[22] Wang H, Li R, Wang E, Zhu Z, Zhang J. 2024. CO_2 capture and dissociation on novel Ni/CaO bifunctional materials: a theoretical study. *Greenhouse Gases: Science and Technology* 14:411–426

[23] Zhao P, Wu Y, Yang C, Wang K, Li P, et al. 2025. The catalytic mechanism for H_2 production on MgO-CaO materials through the water gas shift reaction: a DFT study. *Gas Science and Engineering* 134:205543

[24] Fan Y, Lu B, Shen S, Luo C, Li X, et al. 2026. The interface-induced synergistic mechanism: enhanced CO_2 capture and in-situ hydrogenation on CaO–Cu/CeO_2 dual-functional materials. *International Journal of Hydrogen Energy* 200:152914

[25] Cheng S, Cheng X, Wang Z, Yuan N, Wang X. 2025. Synthesis of activated carbon from Zhundong coal and its hydrogen storage application. *International Journal of Coal Science & Technology* 12:84

[26] Shi W, Li R, Yang H, Kong D, Chen Q. 2025. Influence of Cr- and Co-doped CaO on adsorption properties: DFT study. *Molecules* 30(13):2820

[27] Wang N, Guo X, Ma S, Feng Y. 2023. Understanding the synergistic effect of Ni/Al_2O_3 on CO_2 adsorption and sintering properties of CaO in sorption-enhanced steam reforming process. *Fuel* 341:127766

[28] Guo SJ, Tian XK, Yan J, Ju SH, Zhao CY. 2024. Performance enhancement mechanisms of calcium-based thermochemical energy storage compounds: insights from first-principles and experimental investigations. *Journal of Materials Chemistry A* 12:14129–14147

[29] Ma X, Huang X, Zhang H, Hu X, Feng T. 2023. Effect of calcium aluminates on the structure evolution of CaO during the calcium looping process: a DFT study. *Chemical Engineering Journal* 452:139552

[30] Zhang Y, Fang Y, Chu Z, He Z, Zhao J, et al. 2025. Screening dual variable-valence metal oxides doped calcium-based material for calcium looping thermochemical energy storage and CO_2 capture with DFT calculation. *Journal of Energy Chemistry* 107:170–182

[31] Wang J, Zhao B, Zhu D, Huang F, Zhang W, et al. 2021. Mechanism on catalytic cracking tar with CaO-based catalysts for hydrogen-rich gas by DFT and experiments. *International Journal of Hydrogen Energy* 46:6522–6531

[32] Zou L, Ma L, Wei G, Deng S, Zhao Q. 2026. Catalytic tar cracking over calcium oxide-based bifunctional materials during biomass chemical looping gasification: Experimental and DFT approaches. *Fuel* 418:138736

[33] Delley B. 1990. An all-electron numerical method for solving the local density functional for polyatomic molecules. *The Journal of Chemical Physics* 92:508–517

[34] Delley B. 2000. From molecules to solids with the $DMol^3$ approach. *Journal of Chemical Physics* 113:7756–7764

[35] Yan J, Zhao CY. 2014. First-principle study of CaO/$Ca(OH)_2$ thermochemical energy storage system by Li or Mg cation doping. *Chemical Engineering Science* 117:293–300

[36] Yang P, Sun Z, Duan L, Tang H. 2020. Mechanism of steam-declined sulfation and steam-enhanced carbonation by DFT calculations. *Greenhouse Gases: Science and Technology* 10:472–483

[37] Yan X, Ji X, Chen J, Sun R, Chu H. 2026. Insights into sulfur resistance of Ce-doped CaO in sorption-enhanced steam gasification: A combined DFT and experimental study. *Separation and Purification Technology* 393:137289

[38] Wang Y, Li Y, Yang L, Fan X, Chu L. 2022. Revealing the effects of Ni on sorption-enhanced water-gas shift reaction of CaO for H_2 production by density functional theory. *Process Safety and Environmental Protection* 157:254–265

[39] Yang P, Duan L, Tang H, Cai T, Sun Z. 2018. Explaining steam-enhanced carbonation of CaO based on first principles. *Greenhouse Gases: Science and Technology* 8:1110–1123

[40] Orita H, Uchida K, Itoh N. 2003. Adsorption of thiophene on an MoS_2 cluster model catalyst: ab initio density functional study. *Journal of Molecular Catalysis A: Chemical* 193:197–205

[41] Corva M, Mohamed F, Tomsic E, Rinaldi M, Cepek C, et al. 2019. Learning from nature: charge transfer and carbon dioxide activation at single, biomimetic fe sites in tetrapyrroles on graphene. *The Journal of Physical Chemistry C* 123:3916–3922

[42] Erans M, Manovic V, Anthony EJ. 2016. Calcium looping sorbents for CO_2 capture. *Applied Energy* 180:722–742